International Journal of Heat and Mass Transfer 251 (2025) 127299

Contents lists available at ScienceDirect

International Journal of Heat and Mass Transfer

journal homepage: www.elsevier.com/locate/hmt

Inception of evaporative dryout for CO_2 in milliscale pipe flows

Giulio Cantini [a,b,*], Desiree Hellenschmidt [b], Camila Pedano [b], Paolo Petagna [b], Carl Sangan [a], Mauro Carnevale [a,b]

[a] Department of Mechanical Engineering, University of Bath, Claverton Down, Bath, BA2 7AY, Bath, United Kingdom
[b] CERN, Geneva, Switzerland

ARTICLE INFO

Keywords:
Boiling CO_2
Two-phase flow
Dryout inception
Millichannels
Liquid film
Stability
Perturbation theory

ABSTRACT

Carbon dioxide is a cost-effective, reliable and environmentally-friendly refrigerant with increasing employment in evaporator design. A clear understanding of the underlying flow physics, coupled with robust prediction of phase change through boiling, is necessary to enable widespread uptake of CO_2 as a coolant. In scenarios such as nuclear reactors or thermal management in silicon detectors (*e.g.*, Large Hadron Collider at CERN), employing saturated CO_2 in milliscale pipes introduces further uncertainties in the design process, particularly regarding its behaviour at high vapour quality. During the phase change process, the fluid exhibits an abrupt decrease in the heat transfer coefficient. Such a condition, known as the *onset of dryout*, can lead to potentially catastrophic overheating. Two opposing behaviours are observed in the available literature concerned with the onset of dryout, coined in this study as the δ^- and δ^+ regimes. The δ^- regime exhibits decreasing dryout vapour quality with mass flux, while the δ^+ regime, *which is more relevant to CO_2 in millichannels*, yields an increasing dryout vapour quality with mass flux. A detailed experimental campaign was conducted at CERN providing unprecedented insight into the phenomena resulting in the inception of dryout. A new theoretical model based on small perturbation theory was developed to accurately predict the dryout phase in the δ^+ regime. This study provides *general* theory to predict dryout, which is validated with specifically-acquired data and the wider literature; to the authors' knowledge *all* comparable theories fail to extend their applicability beyond the proposers own datasets. Our new theory is independent from the saturation temperature and heat flux, enabling future investigations to be conducted at a single value of the aforementioned quantities, while permitting extrapolation of the trends to a general parameter set. This unique versatility provides a new framework for the design of carbon-dioxide evaporators with novel cooling architectures.

1. Introduction

In recent years, boiling CO_2 has been increasingly employed as a refrigerant. As highlighted in [1], boiling CO_2 offers numerous advantages over synthetic refrigerants. Its cost-effectiveness, reliability, and minimal Global Warming Potential render CO_2 an environmentally-friendly fluid. The high working pressure and low liquid/vapour density ratio of CO_2 make it well-suited for efficient heat exchange in milliscale diameter pipes and for saturation temperatures (T_{sat}) in the $-40/-10$ °C. Additionally, its non-toxic, non-combustible, and non-corrosive properties are pivotal for safety considerations. Furthermore, its resistance to radiation makes it an ideal candidate for cooling applications in particle physics detectors.

Research at the Large Hadron Collider (LHC) at CERN demands ongoing upgrades of electronic components, such as intricately layered silicon Detectors, necessitated by a persistent rise in Hadron beam density. For specifics regarding the Compact Muon Solenoid (CMS) and Atlas detectors, refer to [2,3] respectively. These upgrades target improved performance under increased radiation levels and advancements in data response rate and resolution. The consequence of these upgrades is an amplified electrical power installation, resulting in increased thermal dissipation. Consequently, a more effective thermal management strategy for detector cooling becomes imperative. Furthermore, for silicon detectors, continuous operational thermal management is essential within a temperature range spanning +15°C to −30°C or lower.

Due to its aforementioned benefits, boiling CO_2 is typically employed as a refrigerant in LHC heat exchangers, particularly in the intricate channel network of the secondary circuit, a feature highlighted in [4]. In the context of CMS design, this arrangement poses geometric constraints. The behaviour of two-phase CO_2 within such microchannel

* Corresponding author at: Department of Mechanical Engineering, University of Bath, Claverton Down, Bath, BA2 7AY, Bath, United Kingdom.
E-mail address: gc803@bath.ac.uk (G. Cantini).

https://doi.org/10.1016/j.ijheatmasstransfer.2025.127299
Received 10 February 2025; Received in revised form 29 April 2025; Accepted 23 May 2025
Available online 20 June 2025

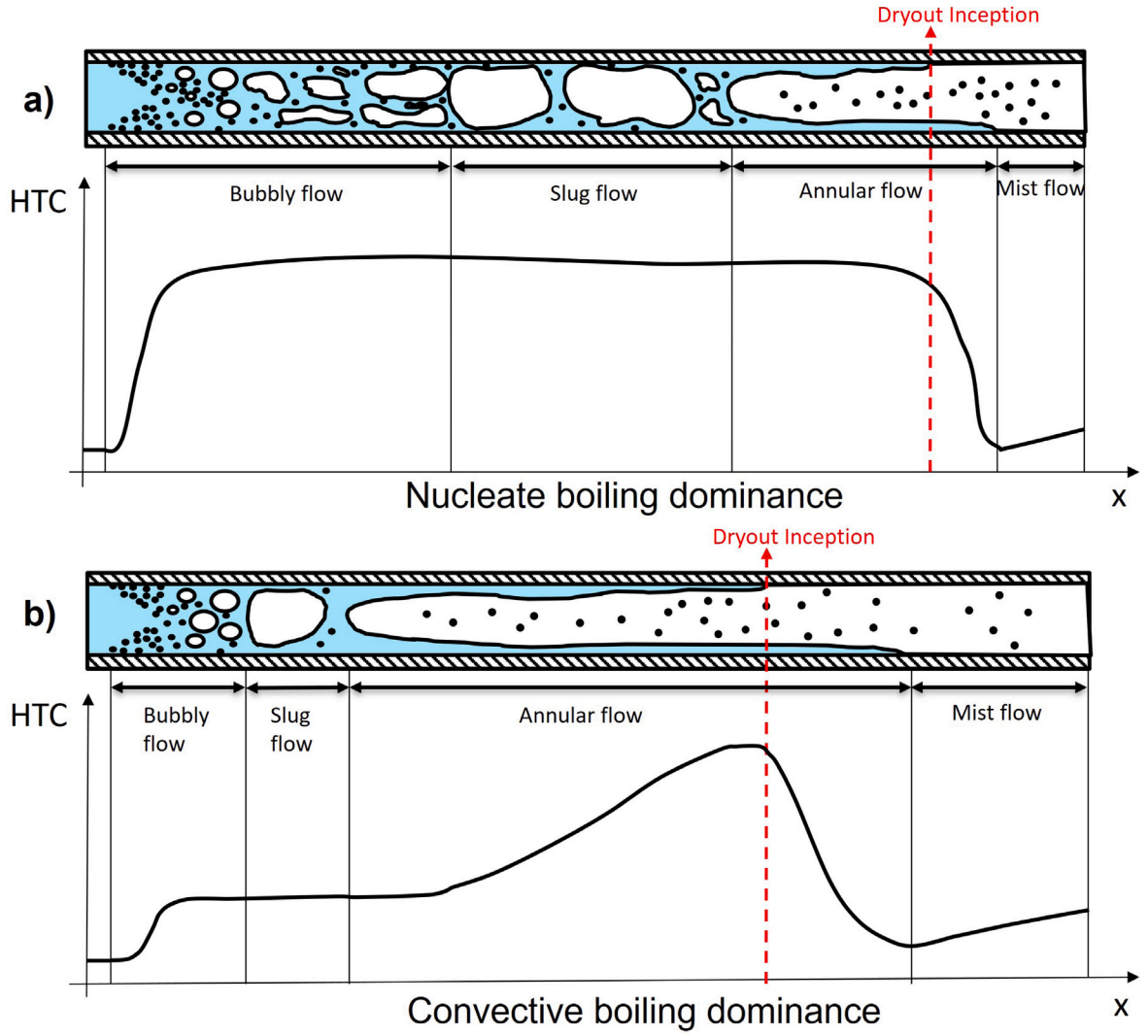

Fig. 1. Two phase flow patterns and qualitative trend of heat transfer coefficient (HTC) for: (a) nucleate boiling dominated heat transfer; (b) convective boiling dominated heat transfer.

networks presents a challenge due to the combined impact of buoyancy and surface tension.

Two-phase flows such as boiling CO_2, exhibit a range of flow patterns and fluid dynamic phenomena at the vapour-liquid interface, illustrated in Fig. 1. These different patterns dictate fluid mechanic and thermodynamic behaviour, characterised by interaction mechanisms such as buoyancy, surface tension, heat and mass transfer. Understanding these mechanisms is crucial when evaluating pressure drop and Heat Transfer Coefficients (HTCs) within the microchannels.

The transition between annular and mist flow patterns is of particular importance for systems like nuclear reactors and silicon Detectors. Annular flow features a continuous interface separating the liquid and vapour phases, leading to high HTCs and pressure drops. Conversely, mist flow involves the dispersion of liquid droplets in the vapour phase, resulting in lower HTC and pressure drop due to reduced thermal conductivity and viscosity. For more details on two-phase flow patterns, refer to [5]. Loss of contact between the heated wall and liquid film reduces heat transfer efficiency, potentially resulting in catastrophic consequences like surface melting, as noted in [6]; this condition is known as "dryout".

Heat transfer in two-phase flows operates via two distinct mechanisms: nucleate and convective boiling. The mechanisms are described in [7] and shown schematically in Fig. 1. Nucleate boiling is dominant at low vapour qualities (x) where a broadly constant HTC is observed; nucleate boiling is independent of mass flux. Elevated saturation temperatures augment nucleate boiling due to reduced surface tension and latent heat. The relative importance of convective boiling heavily relies on mass flux and vapour quality. At constant mass flux, lower saturation conditions correlate with increased flow velocity (lower density), thereby enhancing heat transfer.

To account for the relative contribution of heat transfer mechanisms, [8] propose three contiguous thermal regimes dependent on vapour quality and the Boiling number $\mathrm{Bo} = q/(h_{gl}D)$:

- Low vapour quality ($x < 0.1$): where nucleate boiling dominates.
- High vapour quality ($x > 0.1$) and $Bo > 1.1 \times 10^{-4}$: where both mechanisms (nucleate and convective boiling) significantly contribute.
- High vapour quality ($x > 0.1$) and $Bo < 1.1 \times 10^{-4}$: where convective boiling dominates.

The evaluation of vapour quality at the onset of dryout (x_{dry}) is pivotal when designing cooling systems; the subsequent reduction in HTC influences pressure drops. [9] identified two theoretical trends in CO_2 dryout vapour quality based on mass flux. The two regimes are coined δ^+ and δ^- by the current authors and are defined henceforth as:

- δ^+ **Regime**: x_{dry} increases with rising mass flux G, $\frac{\partial x_{dry}}{\partial G} > 0$. Although less frequently observed in the literature, some instances of this behaviour are documented in [8,10].
- δ^- **Regime**: x_{dry} decreases with increasing mass flux G, $\frac{\partial x_{dry}}{\partial G} < 0$. This regime is widely reported in the literature and informs typical flow pattern maps in the field, typified by [11,12].

The flow pattern map proposed by [12] is considered the most robust for CO_2 but represents solely Regime δ^- behaviour; correlations informed by the δ^- regime will result in an underestimation of x_{dry} when Regime δ^+ behaviour is present. The transition mechanism between the two behaviours is not yet understood.

To determine whether behaviour is in accordance with the δ^- regime or δ^+ regime [10] define a transition mass flux G_{trans} whereby x_{dry} exhibits δ^+ behaviour for $G > G_{trans}$. However, their experimental campaign with 1 mm diameters did not confirm the validity of the G_{trans} hypothesis.

Revellin et al. [9] proposed a phenomenological model based on a system of differential equations (continuity, momentum, energy, and Young–Laplace equation) for liquid and vapour phases. They establish the transition criterion by detecting Kelvin-Helmoltz instabilities at the liquid-vapour interface. This model computes the transition mass flux mentioned by [10] under the assumption that the transition occurs at a threshold value of the liquid-film Reynolds number.

The model proposed by [9] disregards the wall heat flux; however, an experimental study conducted by [8] established an empirical correlation for x_{dry} on a 0.5 mm internal diameter pipe, highlighting the relative importance of the wall heat flux in the δ^+ regime. Moreover, [8]'s findings do not confirm the threshold transitional mass flux proposed by [10].

Kim and Mudawar [7] present a purportedly *general* correlation based on an extensive experimental database, concerned with a variety of pipe diameters, fluid properties and saturation conditions. This correlation was refined by [13] using machine-learning optimisation techniques.

It is crucial to differentiate between these approaches: while [9] offer a physically-informed explanation for the phenomenon, they overlook wall heat flux. Conversely, data-driven correlations like those by [7,8], and [13] are uninformed by the underlying flow physics.

Importantly, all theoretical approaches presented in the open literature fail to model the compound effects of all contributing physical parameters, as stressed by [14].

Morse et al. [15] conducted an experimental investigation of the dryout phenomenon and developed a theoretical model based on the frequency of de-wetting and re-wetting of the pipe wall. The campaign focussed on the δ^- regime demonstrated reasonable agreement with experimental data.

This study presents a stability analysis of the liquid-vapour interface in annular flow, governing the behaviour in the δ^+ regime and reveals that x_{dry} is driven by the Bo/We ratio. An extensive experimental assessment of HTC and x_{dry} for boiling CO_2 in a 1 mm internal diameter pipe is reported and a novel correlation is proposed; the robustness of the new modelling approach is demonstrated through comparison with the [8] data. The new theory is independent from the saturation temperature and heat flux, providing a versatile framework for the design of carbon-dioxide evaporators with novel cooling architectures.

2. Experimental facility

The CERN experimental facility comprises of two interconnected sub-systems: a stand-alone refrigeration system and a millichannel cooling loop; the latter is encapsulated within a vacuum chamber. In the interest of brevity, only a brief description of the test facility is presented here; the interested reader is directed to [16,17] for further details, including preliminary validation of the experimental setup with single-phase flow.

The stand-alone refrigeration system is a derivative of the 2PACL system developed by CERN and reported in [18,19]. The refrigeration system is comprised of primary and secondary circuits, as shown in Fig. 2a; the experimental *test circuit* is described separately below. The primary circuit employs an external R404 A chiller to condense the CO_2 in the secondary circuit through a single-pass heat exchanger. The condensed CO_2 then passes through a valve and undergoes an isenthalpic transformation prior to entry into the test section, as shown in Fig. 2b. Pressure and temperature are regulated within the circuit using a two-phase accumulator. The refrigeration system is designed to deliver saturated liquid at various saturation temperatures in a range between −25 °C to 20 °C. The flow then circulates through the test section and returns in a post-evaporative, single vapour phase to the secondary refrigerant circuit.

The test circuit is housed within a vacuum vessel, ensuring thermal isolation from the laboratory and near-adiabatic test conditions. The saturation temperature and static pressure of the flow in the test circuit is monitored at six locations (denoted MP1 to MP6 in Fig. 2b). Resistance thermometers (RTD, PT100, 4-wire configuration) were used to assess saturation temperature; an absolute pressure transducer(General Electrics UNIK 5000) is installed outside the vessel for an accurate determination of the absolute pressure. Once the fluid enters the vacuum vessel the first measurement location (MP1) is used to verify that the appropriate fluid properties are supplied to the test circuit.

The working fluid subsequently passes through an electric pre-heater (VISHAY RPS500); isothermal heating is ensured by mounting the heater onto a copper block through which passes a coiled fluid conduit. The pre-heater is used to control the vapour quality at the inlet of the test section, as follows:

$$x_{in} = \frac{Q}{\dot{m} h_{gl}} \tag{1}$$

where Q is the power input to the heater (J/s), $\dot{m}$ is the mass flow rate (kg/s) and h_{gl} is the latent heat (J/kg). Immediately downstream of the heater, temperature and pressure are assessed at MP3 to ensure that the appropriate test condition has been reached before the fluid enters the actual test section. An orifice is installed upstream of the test section to promote pressure uniformity at the inflow boundary; experiments in the absence of an orifice demonstrated consistent qualitative trends in the results, albeit with larger pressure fluctuations at the inlet.

Fast-response K-type thermocouples are used to asses the axial distribution of wall temperature along the test section. Contact between the thermocouple beads and the outer surface of the millichannel is ensured by compressing the hot-junction under a stainless steel bush within a specifically-designed Tufnol clamp, as shown in Fig. 3. The thermocouples were calibrated against a Platinum standard reference thermometer (Fluke, HART 5626-12) to an accuracy of +/−0.1° C. Twelve thermocouples were spaced equidistantly along the test specimen. Three equispaced copper electrodes (identified on Fig. 2b) are used to impart a constant heat flux to the test specimen using the Joule effect; the two anodes are connected to the pipe extremities and the cathode is located in the centre of the test section. The effective length used to calculate the heat input required is 180 mm for a 1 mm pipe bore. The heat power produced by Joule effect was controlled by a resistive circuit (also known as resistive heating) $W_{joule} = RI^2$, where I is the electric current (in Amperes), R is the resistance (in Ohms). The heat flux q is calculated as the ratio between the provided heat W_{joule} and the wall surface:

$$q = \frac{W_{joule}}{\pi D_{in} L_{heated}} \tag{2}$$

Once located inside the vacuum vessel, the twelve clamped thermocouples were assessed for contact efficacy. The creation of a vacuum can lead to high thermocouple yield where the bead becomes unattached from the pipe surface. It is widely reported in the literature that the HTC is independent of vapour quality as $x \to 0$ (*e.g.* [8]);

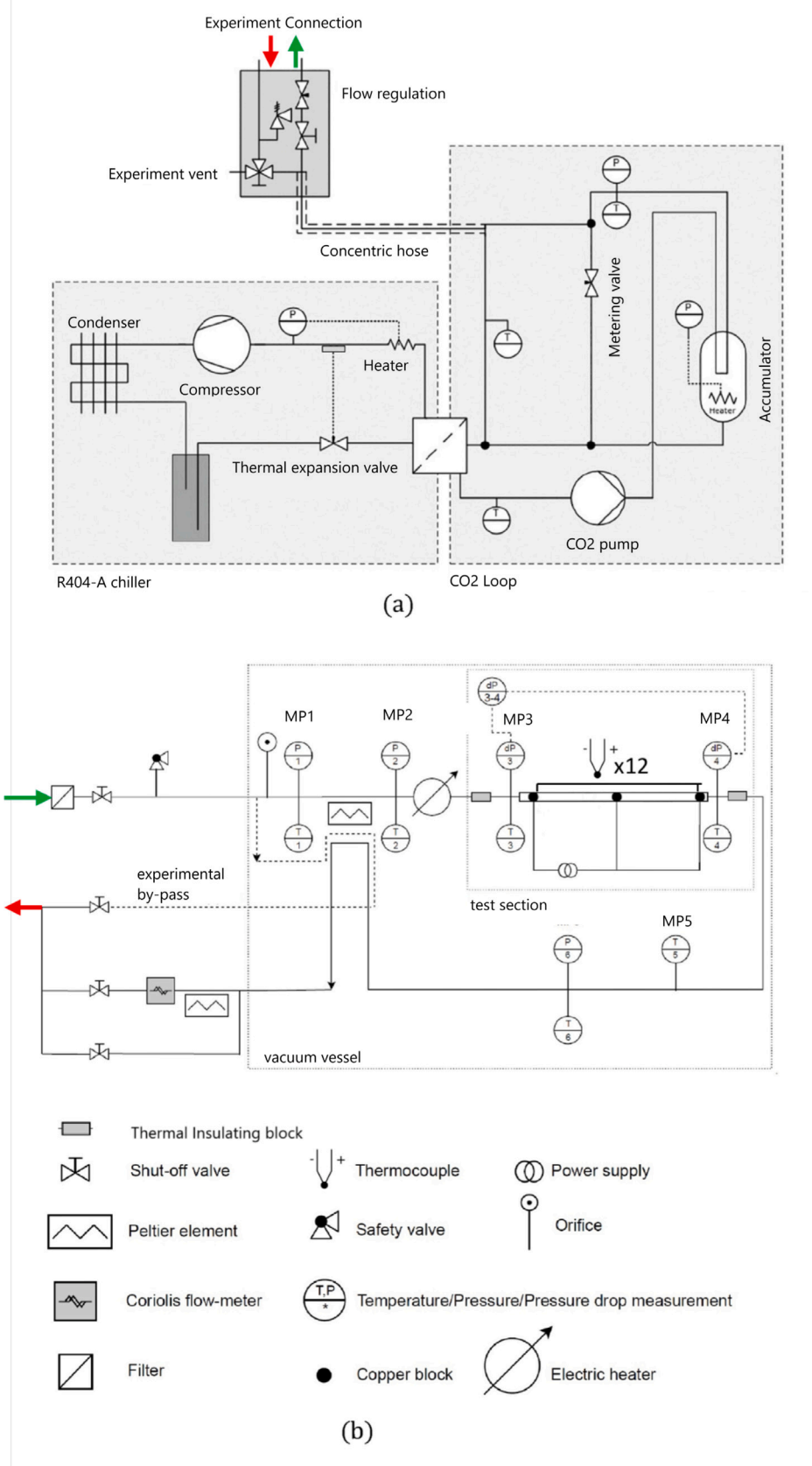

Fig. 2. Schematics of the experimental facility: (a) the 2PACL refrigerant system; (b) the test section.

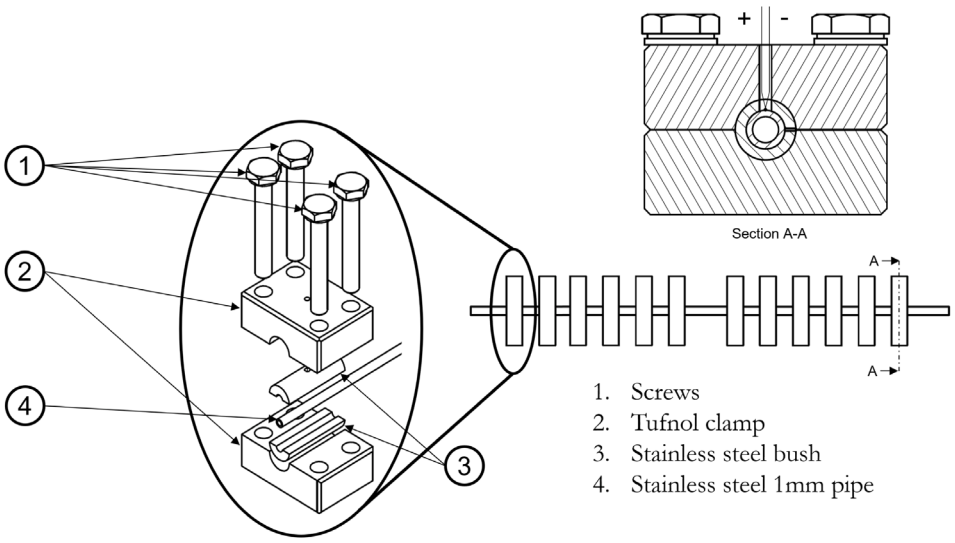

Fig. 3. Schematic of the test section; pipe has a 1 mm internal diameter.

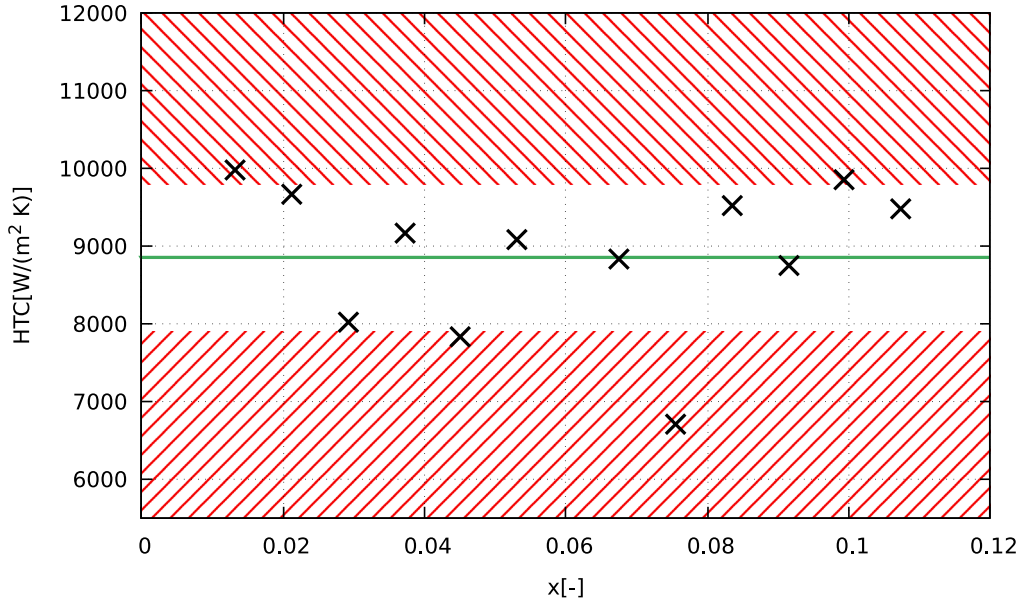

Fig. 4. Assessment of thermocouple yield within a vacuum environment; the symbols represent the measured HTCs for an example test case (G = 800 kg/m^{2}s, T_{sat} = 0°C and q = 30 kW/m^2), the green line is the average HTC and the red shaded regions indicate measured data that falls outside of one standard deviation from the mean.

the test cases without pre-heating (*i.e.* $x \rightarrow 0$) were used to identify thermocouples with a systematic error greater than the root-mean square of the measured data set. An example of this procedure is shown in Fig. 4, where the thermocouple yield for this condition was 33% (*i.e.* four out of twelve thermocouples were discarded).

Once the fluid exits the test section at MP4, the pressure drop is determined between the inlet and the outlet using a differential pressure transducer (Endress+Hauser, DeltabarM PMD75B). A Coriolis flow meter (Rheonik, RHM015) is used to assess the mass flow-rate within the test circuit, acquired at a downstream location once complete vaporisation of the flow has occurred.

The experimental campaign comprises three different saturation temperatures, four different mass fluxes and two different heat fluxes. For each test condition the inlet vapour quality is conditioned by the pre-heater until the dryout condition is reached. The onset of dryout is indicated by a sudden increase of the measured wall temperature. All test cases are shown in Table 1, with those cases in red identifying the presence of a condition where both nucleate and convective boiling significantly contribute, as suggested by [8].

3. Results and discussion

The vapour quality, x, is evaluated at each axial coordinate, z, considering the conservation of energy:

$$x(z) = x_{in} + \frac{4q}{GD_i h_{gl}} z \tag{3}$$

where G is the mass flux and h_{gl} is the latent heat. The local heat transfer coefficient (HTC) is evaluated based on temperature measurements from spatially-resolute thermocouple installations, as follows:

$$HTC(z) = \frac{q}{T_{w,o}(z) - T_{sat}(z) - \Delta T_w} \tag{4}$$

$T_{w,o}(z)$ and $T_{sat}(z)$ are the measured outer wall temperature and the fluid temperature at location z, respectively. A linear decrease in pressure between MP3 and MP4 is assumed; accordingly the saturation temperature $T_{sat}(z)$ falls with axial distance from the pipe inlet. ΔT_w is the temperature difference between the external and internal wall of

Table 1
Test matrix.

	$T_{sat} = -15$ °C		$T_{sat} = 0$ °C		$T_{sat} = 15$ °C	
	$q = 5 \frac{kW}{m^2K}$	$q = 30 \frac{kW}{m^2K}$	$q = 5 \frac{kW}{m^2K}$	$q = 30 \frac{kW}{m^2K}$	$q = 5 \frac{kW}{m^2K}$	$q = 30 \frac{kW}{m^2K}$
$G\left[\frac{kg}{m^2s}\right]$	500	500	500	500	500	500
	800	800	800	800	800	800
	1200	1200	1200	1200	1200	1200
	2000	2000	2000	2000	2000	2000

Table 2
Measurement equipment uncertainties.

Measurement	Device	Calibration range	Uncertainty
ΔP	Diff. press. trans	0–3 bar	+−0.005% of FS
P_1	Abs. press. trans.	0–100 bar	+−0.04% of FS
P_2	Abs. press. trans.	0–100 bar	+−0.04% of FS
P_4	Abs. press. trans.	0–100 bar	+−0.04% of FS
P_{vacuum}	Vacuum gauge	5E-9–1000 mbar	+−30% of reading
T_{1-6}	RTDPt100	−200 to 600 °C	+−(0.15+0.002[T]) °C
T_{wall}	TC K-type (calibr.)	−50 to 250 °C	+−0.2 °C
$\dot{m}$	Coriolis MFM 1	0.03–0.6 kg/min	+−0.2% of reading
$\dot{m}$	Coriolis MFM 2	12–600 g/h	+−0.2% of reading+0.5g/h
$V_{JouleHeater}$	Joule heater: volt meter	0–18 V	+−0.2% +1 digit
$A_{JouleHeater}$	Joule heater: ampere meter	0–20 A	+−0.5% +1 digit
$V_{pre-Heater}$	Pre-heater: volt meter	0–18 V	+−0.2% +1 digit
$A_{pre-Heater}$	Pre-heater: ampere meter	0–20 A	+−0.5% +1 digit

the pipe and it is calculated assuming steady conductive heat transfer:

$$\Delta T_w = \frac{q D_i}{4\lambda_{SS}} \frac{\Phi(1 - \ln\Phi) - 1}{1 - \Phi} \tag{5}$$

where $\Phi = D_o/D_i$, $\lambda_{SS} = 14.4$ W/mK (thermal conductivity of stainless steel) and D_i and D_o are the inner and outer diameter of the pipe, respectively. A steady state conduction does not take into account the production of heat *within* the pipe and unsteadiness in heat transfer. However, the high thermal conductivity, the small thickness of the wall and the fact that only averaged quantities are considered make both negligible. The error in the calculation of HTC is obtained through uncertainty propagation (the interested reader can find further details in [20]). Given a quantity, Y, depending on N different measured quantities, x_i, the variance of $Y(x_1, \ldots, x_N)$ is expressed as

$$\sigma_Y^2 = \sum_{i=1}^{N} \left(\frac{\partial Y(x_1, \ldots, x_N)}{\partial x_i} \right)^2 \sigma_{x_i}^2 \tag{6}$$

Applying the uncertainty quantification to Eq. (4) yields

$$\left(\frac{\sigma_{HTC}}{HTC}\right)^2 = \frac{\sigma_q^2}{q^2} + \frac{HTC^2}{q^2} \left(\sigma_{T_{w,o}}^2 + \sigma_{T_{sat}}^2 + \sigma_{\Delta T_w}^2 \right) \tag{7}$$

where

$$\sigma_{\Delta T_w}^2 = \Delta T_w^2 \left(\frac{\sigma_q^2}{q^2} + \frac{\sigma_{D_i}^2}{D_i^2} \right) + \left(\frac{q D_i}{4\lambda_{SS}} \frac{\Phi(\Phi - \ln\Phi - 1)}{(1 - \Phi)^2} \right)^2 \left(\frac{\sigma_{D_o}^2}{D_o^2} + \frac{\sigma_{D_i}^2}{D_i^2} \right) \tag{8}$$

From Eq. (7) it is apparent how the relative error in HTC is proportional to its magnitude, explaining the high data scattering observed at high HTC conditions.

Table 2 reports the uncertainty and calibration range for each measurement device.

3.1. Influence of mass flux on the heat transfer coefficient

The distribution of HTC as a function of the vapour quality, x, is shown in Figs. 5 and 6, for $q = 30$ kW/m^2 and $q = 5$ kW/m^2, respectively. Data are presented for different saturation temperatures, T_{sat}, and different mass fluxes, G. At the fully saturated liquid condition ($x = 0$), the level of HTC is independent of mass flux; dependency is however observed on the level of heat flux and saturation temperature. This behaviour is attributed to the nucleate boiling occurring in low vapour quality flow regimes, in agreement with [21].

Now consider conditions where $x > 0$. For all cases, a significant and abrupt reduction in the level of HTC is observed at high vapour quality, in accordance with the onset of dryout; the conditions at $T_{sat} = -15$°C and $T_{sat} = 0$°C at $q = 30$ kW/m^2 and $G = 500$ kg/m^{2}s exhibit less abrupt, yet equally significant reductions in HTC. The data at high HTC exhibit pronounced scattering in accordance with the larger relative error in temperature measurement at high HTC values. For $T_{sat} = 0$°C at $q = 30$ kW/m^2 and $G = 500$ kg/m^{2}s the magnitude of the HTC appears higher than the consistent cases with elevated mass fluxes. This apparent contradiction is attributed to nucleate boiling being suppressed at the high flow-rate condition, and in accordance resulting in a disproportionately low HTC despite the higher mass flux.

The independence of HTC with mass flux seen for $x = 0$, is equally observed for $0 < x < x_{dry}$ for cases at elevated saturation temperatures. At $T_{sat} = 0$°C, mass flux independence extends up to $x = 0.4$ for high heat flux, i.e. $q = 30$ kW/m^2 and up to $x = 0.2$ for low heat flux, i.e. $q = 5$ kW/m^2. For $T_{sat} = 15$°C the independence extends up to $x = x_{dry}$. This behaviour is consistent with the dominance of nucleate boiling, in accordance with the Introduction. Here, the nucleate boiling is attributed to the δ^- regime. The case with $T_{sat} = 15$°C and $q = 30$ kW/m^2 is the sole test case where δ^- regime is observed. At $T_{sat} = -15$°C, no independence with mass flux is observed beyond $x = 0$.

3.2. Influence of heat flux on the heat transfer coefficient

The HTC data are replotted as function of vapour quality in Figs. 7 and 8 for G = 800 kg/m^{2}s and G = 2000 kg/m^{2}s, respectively, in order to aid direct comparison between conditions of high and low heat flux. As the experiments are carried out at saturated conditions, the temperature of the fluid is constant and equal to the saturation temperature, *i.e.* it is not affected by the level of heat flux. The experiments corroborate the implied proportionally between HTC and q, as expressed in Eq. (4).

3.3. Influence of saturation temperature on heat transfer coefficient

The HTC data are replotted a third time, now as a function of vapour quality, x, in Figs. 9 and 10 for $q = 5$ kW/m^2 and $q = 30$ kW/m^2, respectively. In each plot HTC is directly compared for different saturation temperatures. In Fig. 10(a), HTC is seen to increases with T_{sat}, for conditions close to saturated liquid, where reducing surface tension enhances bubble nucleation, as shown by [14]. Latent heat decreases with saturation temperature, T_{sat}. Consequently, localised heat transfer is

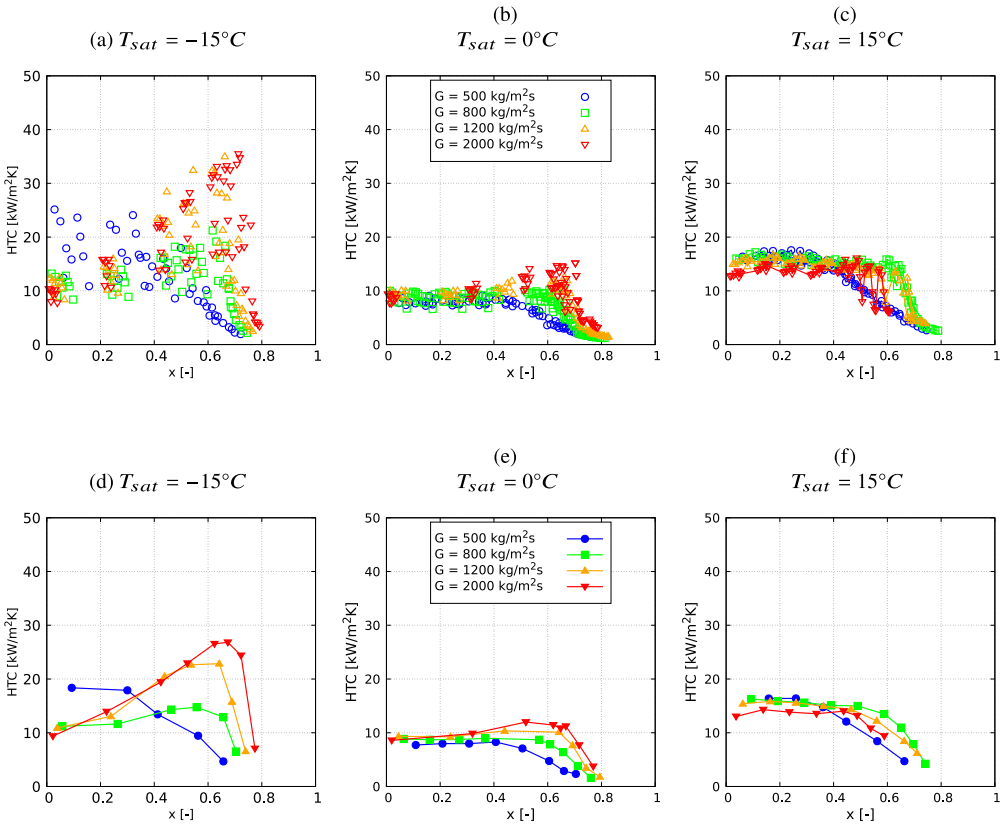

Fig. 5. HTC as a function of x for different T_{sat} and $q = 30$ kW/m^2; (a–c) measured data, (d–f) averaged values for each pre-heated test condition.

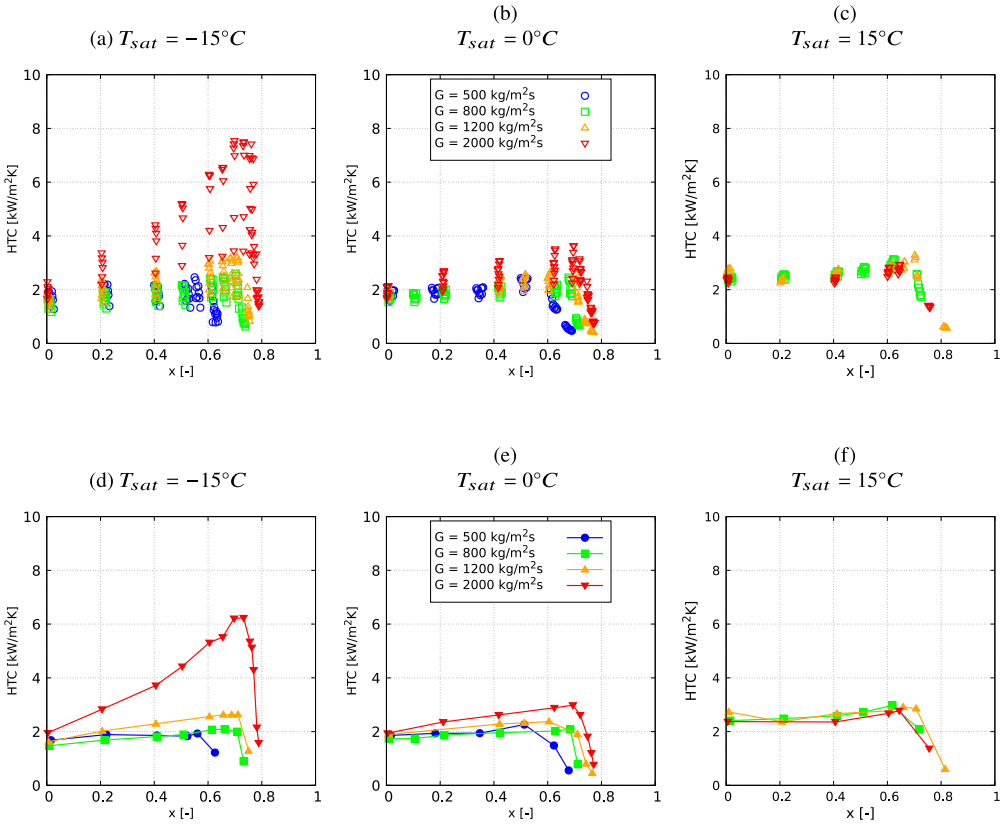

Fig. 6. Measured (a–c) and averaged (d–f) HTC as a function of x for different T_{sat} and $q = 5$kW/m^2.

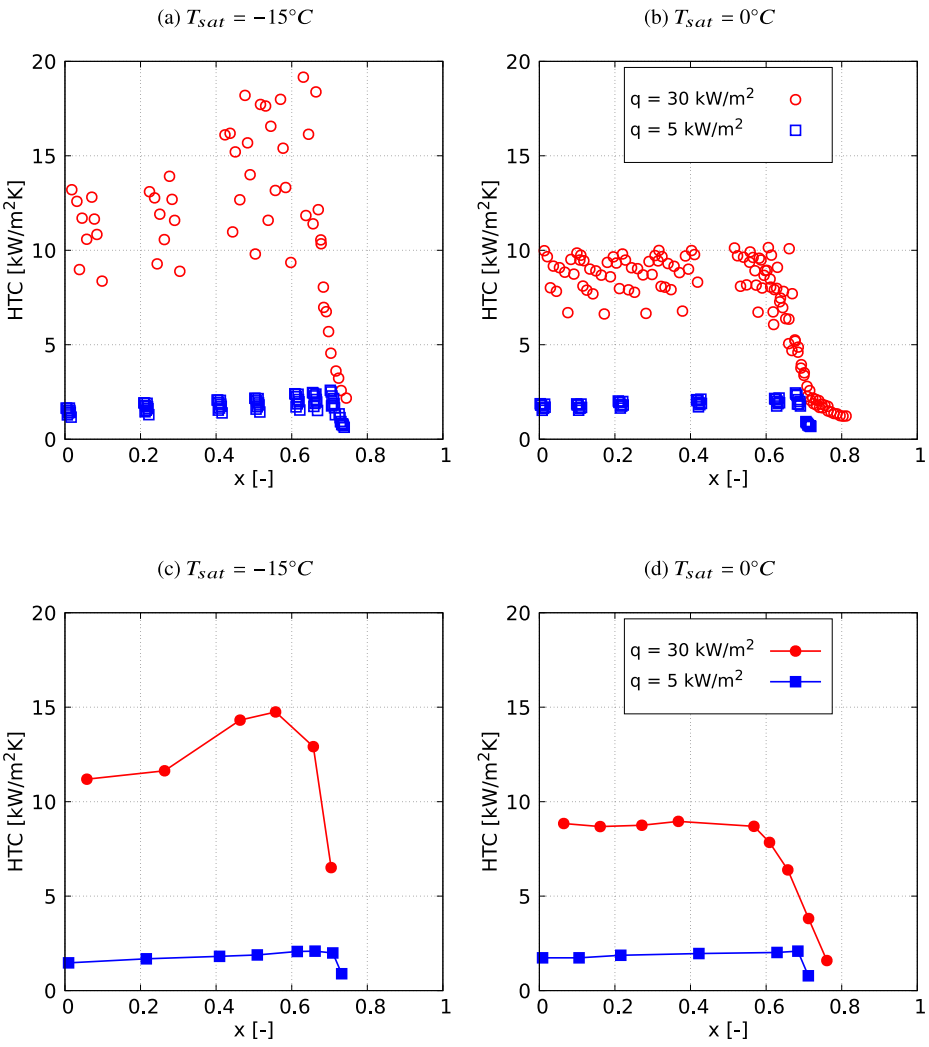

Fig. 7. Measured (a–b) and averaged (c–d) HTC as a function of x for different q and T_{sat}; $G = 800$ kg/m^{2}s.

augmented by the increasing presence of vapour, generated through the boiling process. In turn, for conditions at high vapour quality, the level of HTC increases due to convective evaporation. This effect is magnified at lower T_{sat}, where HTC exhibits a strong positive correlation with x, prior to the onset of dryout; for low T_{sat} the correspondingly lower vapour density results in a higher flow velocity enhancing the local convective heat transfer. Lowering the saturation temperature shifts the dominant behaviour from nucleate boiling to convective boiling, confirming the hypothesis of [8].

3.4. Dryout vapour quality

The characteristic dryout vapour quality is determined from data acquired from all installed thermocouples. For each thermocouple dataset, the onset of dryout is indicated by an abrupt reduction in HTC; the dryout vapour quality corresponds to the location of maximum HTC prior to the reduction The dryout onset point determined from each dataset is subsequently averaged to provide an overall estimate of the dryout vapour quality at that test condition; an example test case is shown in Fig. 11. The onset point of dryout, x_{dry}, is presented as a function of the mass flux in Fig. 12. The error bars shown in Figs. 12 and 13 are determined from the variance of the solid data points in Fig. 11.

At the lowest mass flux (*i.e.* $G = 500$ kg/m^{2}s) a lower saturation temperature results in earlier onset of dryout. This is consistent with the observed HTC behaviour: for low mass flux, the heat transfer coefficient is augmented at higher T_{sat}. Similarly to HTC behaviour, for higher mass flux a lower saturation temperature results in a higher x_{dry}; for high mass flux the higher latent heat and the lower vapour density, due to a lower T_{sat}, enhance the convective evaporation.

Behaviour indicative of the δ^- regime is observed for $T_{sat} = 15$ °C and $q = 30$ kW/m^2, as shown in Fig. 12(b). Here x_{dry} decreases with increasing mass flux, consistent with the flow pattern maps proposed by [12]. In agreement with Section 3.1, the relative dominance of nucleate boiling is inextricably linked to δ^- behaviour. Behaviour commensurate with the δ^+ regime is observed for all remaining cases: increasing mass flux promotes delayed onset of dryout.

In Fig. 13 the dryout vapour quality is plotted as a function of T_{sat} for different heat and mass fluxes. For the lowest mass flux (*i.e.* $G = 500$ kg/m^{2}s), the dryout vapour quality broadly increases with T_{sat} for all tested heat fluxes. For higher mass fluxes the trend progressively reverses; at $G = 2000$ kg/m^{2}s, x_{dry} *decreases* with T_{sat} for both tested heat fluxes. For all cases, earlier inception of dryout exists for the higher heat flux condition, as shown in Fig. 13 and in agreement with [8]. Phenomenologically, this is attributed to transition from δ^+ to δ^- behaviour as q is increased. The former is associated with evaporative convection, without bubbles present at the interface; the latter is associated with higher levels of heat flux leading to nucleation.

3.5. Stability analysis

Albeit unclassified as the δ^+ regime coined in this study, the data of [7,8] exhibit an increasing x_{dry} with rising mass flux at conditions

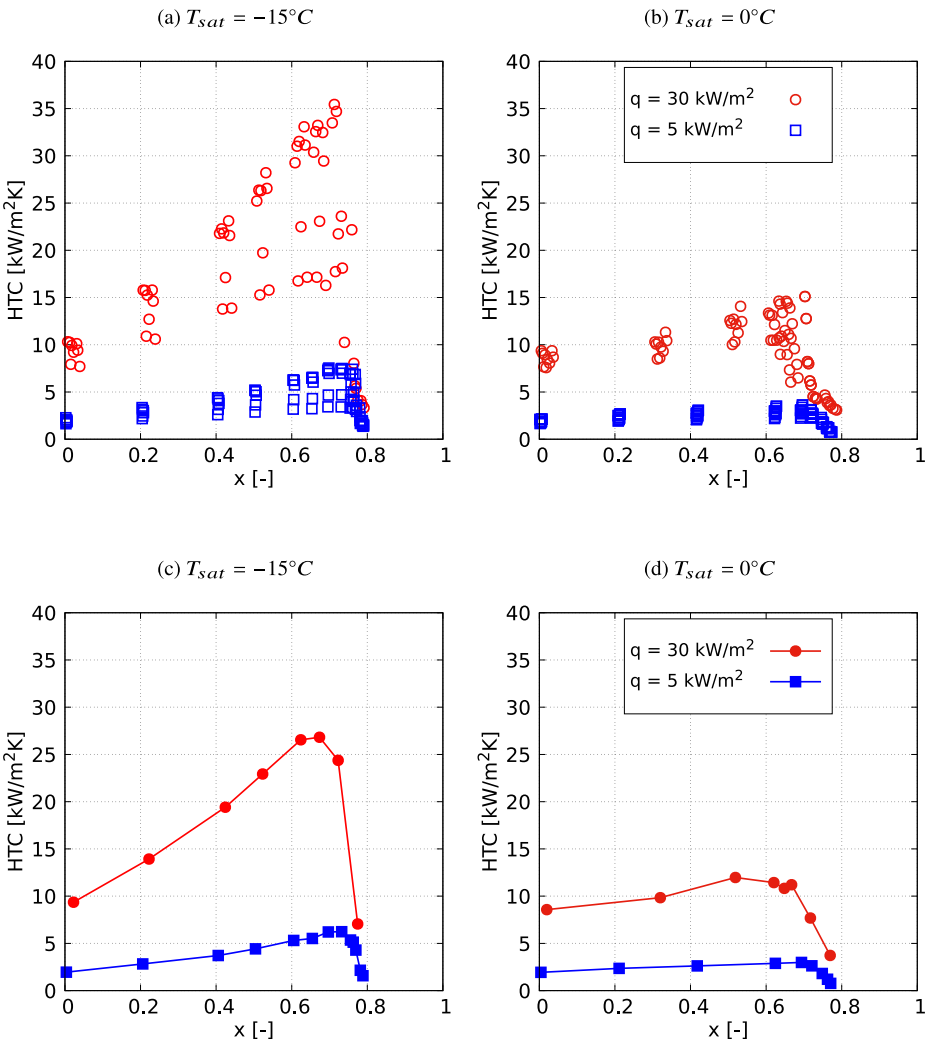

Fig. 8. Measured (a–b) and averaged (c–d) HTC as a function of x for different q and T_{sat}; $G = 2000$ kg/m^{2}s.

pertaining to low heat flux, low saturation temperature and for small pipe diameters. The effect of gravity is omitted owing to the high surface tension at small scale, coupled with the low saturation temperature characteristic of the δ^+ regime. Such conditions support the assumption of a smooth interface between the vapour and liquid phases in annular flow, as stressed by [22,23]. The hypothesis is strengthened when considering that evaporative convection dominates in the Delta+ regime, promoting an absence of nucleation at the interface.

Furthermore as the diameter of pipe is small the velocity of the liquid flow is moderated for the tested mass fluxes. This makes the thickness of the boundary layer within the liquid film very small and the sole forces acting on liquid phase are due to the molecular viscosity, thus liquid-flow can be considered laminar.

Small perturbation theory is applied to the steady-state solution (for further details the reader can refer to [24]) following the method proposed by [25]. Perturbation theory is widely used to solve interface stability problems, for example by [26,27]. Such theory has been successfully applied to interfacial waves occurring in annular flow by [28]; the study focused on oil-water annular flow *without* consideration of heat and mass transfer, nevertheless the instabilities at the interface were successfully characterised in two-dimensional form. Successful implementation of a two-dimensional simplification to the flow pattern was also presented by [29]. The relatively small thickness of the liquid film compared to the pipe diameter — consistent with the high value of void fraction, α, for annular flow at high vapour quality — also renders the problem ideal for modelling in reduced dimensional form, as shown by [24]. This study therefore assumes a two-dimensional stability problem *with* consideration of heat and mass transfer across the liquid-vapour interface.

According to perturbation theory, given $A(x, y)$ as a steady-state solution for the quantity a the perturbed solution is written as $a = A + \hat{a}(y)\exp(ikz + nt)$ with $k \in \mathbb{R}$ and $n \in \mathbb{C}$. The incompressible Navier–Stokes equations are as follows

$$\frac{\partial u}{\partial t} + u\frac{\partial u}{\partial z} + v\frac{\partial u}{\partial y} = -\frac{\partial p}{\partial z} + \frac{1}{\mathrm{Re}}\left(\frac{\partial^2 u}{\partial z^2} + \frac{\partial^2 u}{\partial y^2}\right) \tag{9}$$

$$\frac{\partial v}{\partial t} + u\frac{\partial v}{\partial z} + v\frac{\partial v}{\partial y} = -\frac{\partial p}{\partial y} + \frac{1}{\mathrm{Re}}\left(\frac{\partial^2 v}{\partial z^2} + \frac{\partial^2 v}{\partial y^2}\right) \tag{10}$$

$$\frac{\partial u}{\partial z} + \frac{\partial v}{\partial y} = 0 \tag{11}$$

Considering that the steady-state solution already satisfies this set of equations, and neglecting all terms with an order greater than 1, Eqs. (9)–(11) can be rewritten to obtain the Orr–Sommerfeld Equation

$$(n + ikU)\left(\frac{\mathrm{d}^2}{\mathrm{d}y^2} - k^2\right)\hat{v} - ik\frac{\mathrm{d}^2 U}{\mathrm{d}y^2}\hat{v} = \frac{1}{\mathrm{Re}}\left(\frac{\mathrm{d}^2}{\mathrm{d}y^2} - k^2\right)^2\hat{v} \tag{12}$$

where $\hat{v}$ is the perturbed velocity in the y-direction, U is the steady-state velocity, Re is the Reynolds number and k is the wavenumber. Eq. (12) is typically solved for single-phase flows in order to find the critical Reynolds number which denotes the transition between laminar and turbulent regimes, as shown by [30]. The interested reader is

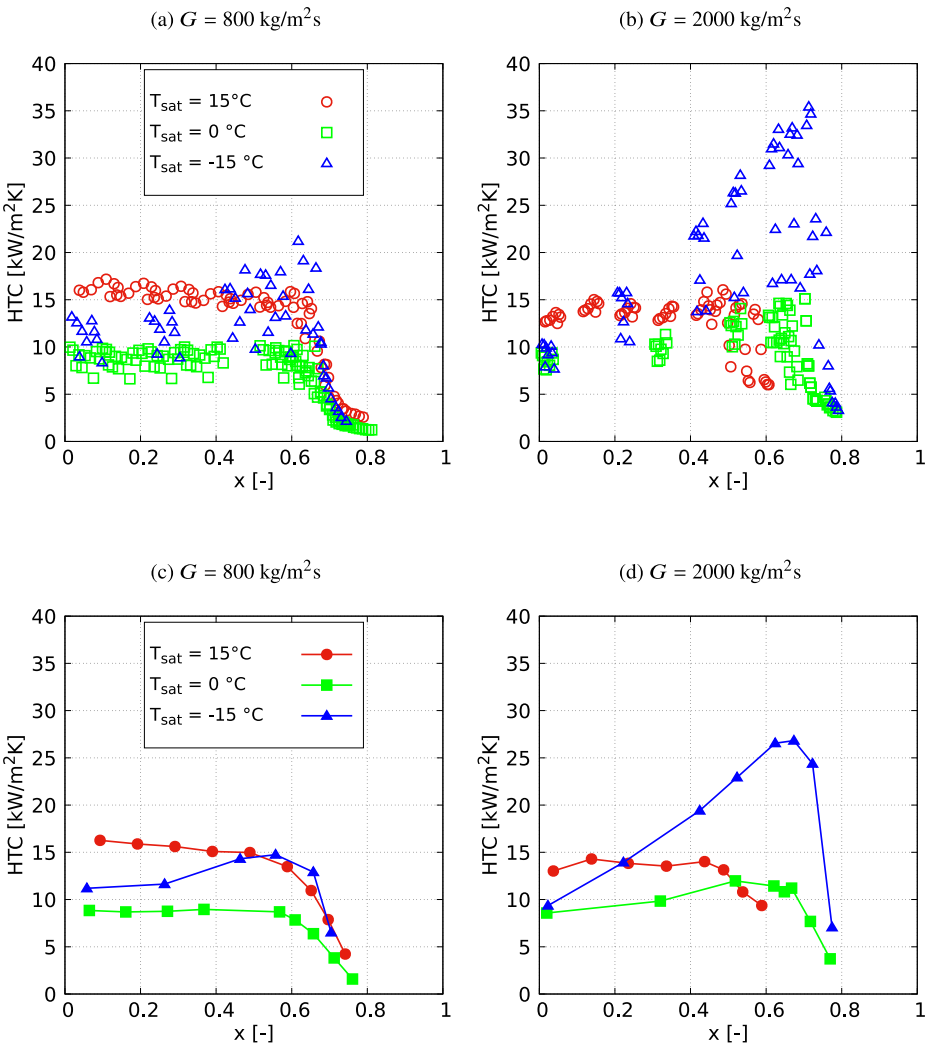

Fig. 9. Measured (a–b) and averaged (c–d) HTC as a function of x for different G and T_{sat}; $q = 30$ kW/m^2.

referred to [31,32] for appropriate numerical methods used to solve the Orr–Sommerfeld equation.

With reference to Fig. 14, the Orr–Sommerfeld equation is expressed for both the liquid and gas phases; each phase has different viscosity, density and steady-state velocity. The eigenvalue n for Eq. (12) yields non-trivial solutions in accordance with the prescribed boundary conditions. If $\Re(n) > 0$, the fluctuating component increases with time, progressively disrupting the liquid-film interface and leading to the inception of dryout. Two differential equations of the fourth order necessitate a set of eight boundary conditions to be solved:

- No slip condition at the wall (Two equations)
- Perturbed velocity equal to steady-state velocity at the pipe axis (Two equations)
- Conservation of mass across the interface (One equation)
- Conservation of energy across the interface (One equation)
- Conservation of momentum across the interface (Two equations)

It is worth noting that a complex problem such this cannot be simply reduced to well-known instabilities like Rayleigh–Taylor, Kelvin–Helmholtz, and Rayleigh-Bénard. Further direct treatment of the generalised mathematical formulation is required to develop a parameter indicative of the inception of dryout. The conservation of momentum across the liquid–vapour interface with respect to z is written as follows

$$\rho_L u_L^* \left(\frac{\partial S^*}{\partial t^*} + u_L^* \frac{\partial S^*}{\partial z^*} + v_L^* \frac{\partial S^*}{\partial y^*} \right) - \tau_{zz}^{*L} \frac{\partial S^*}{\partial z^*} - \tau_{yz}^{*L} \frac{\partial S^*}{\partial y^*} = \\ = \rho_V u_V^* \left(\frac{\partial S^*}{\partial t^*} + u_V^* \frac{\partial S^*}{\partial z^*} + v_V^* \frac{\partial S^*}{\partial y^*} \right) - \tau_{zz}^{*V} \frac{\partial S^*}{\partial z^*} - \tau_{yz}^{*V} \frac{\partial S^*}{\partial y^*} - \\ - \sigma \left(\frac{1}{R_1^*} + \frac{1}{R_2^*} \right) \frac{\partial S^*}{\partial z^*} \tag{13}$$

where ρ_L and ρ_V are the liquid and vapour density, respectively. $S^*(y, z, t)$ is a function such that $S^* = 0$ identifies the liquid-vapour interface, σ is the surface tension and the term $\tau_{ij}^{*\phi}$ is the ij component of the stress tensor for the phase ϕ defined as

$$\tau_{ij}^{\phi} = \delta_{ij} \left(-p + 2\mu_\phi \frac{\partial u_{i,\phi}}{\partial x_i} \right) + (1 - \delta_{ij}) \mu_\phi \left(\frac{\partial u_{i,\phi}}{\partial x_j} + \frac{\partial u_{j,\phi}}{\partial x_i} \right) \tag{14}$$

where δ_{ij} is the Kronecker delta. u_ϕ^* and v_ϕ^* are the axial and normal components of velocity relative to the wall for the phase ϕ. Eq. (13) is evaluated at the interface; R_i^* are the radii of curvature of the interface. The stars denote dimensional terms in Eq. (13), consistent with notation adopted in perturbation theory (see [24]). The following dimensionless variables are defined

$$t = \frac{G}{D\rho_L} t^* \qquad y = \frac{y^*}{D} \qquad x = \frac{x^*}{D}$$

$$u_L = \frac{\rho_L}{G} u_L^* \qquad v_L = \frac{\rho_L}{G} v_L^* \qquad \tau_{ij}^L = \frac{\rho_L D}{\mu_L G} \tau_{ij}^{*L}$$

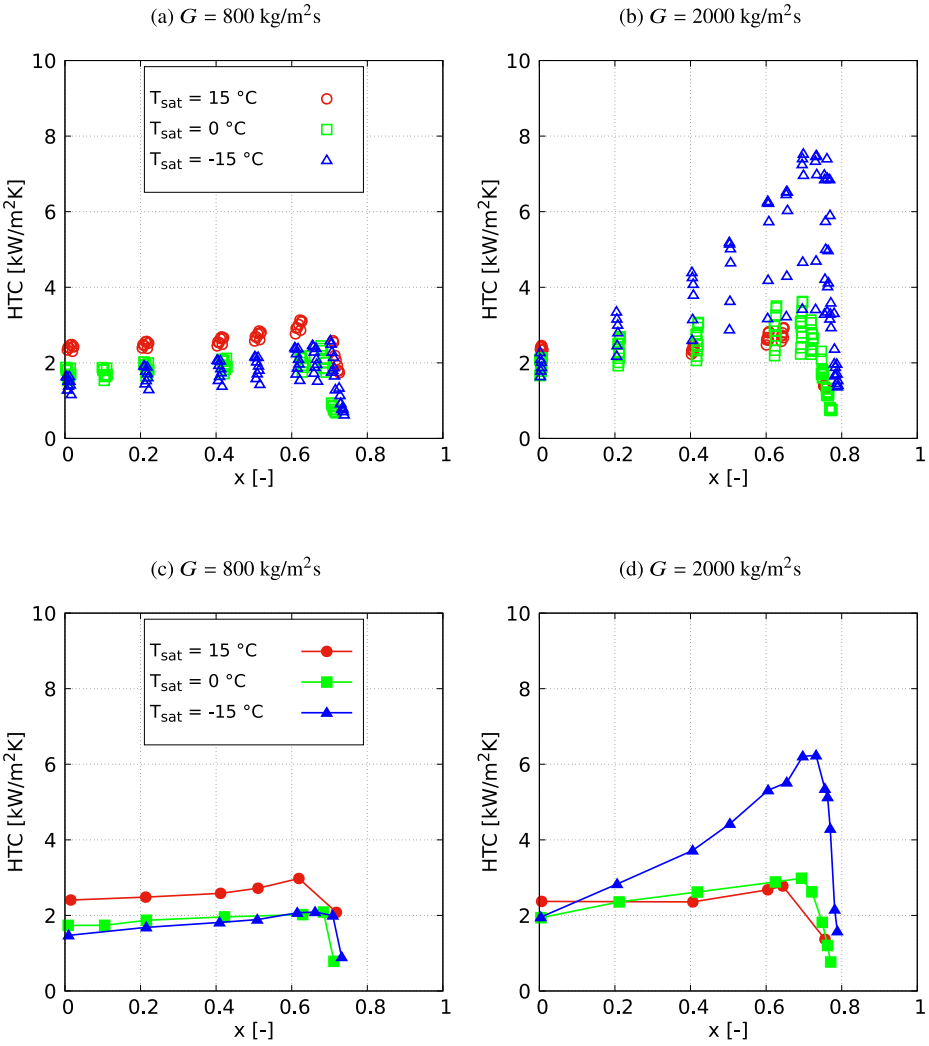

Fig. 10. Measured (a–b) and averaged (c–d) HTC as a function of x for different G and T_{sat}; $q = 5$ kW/m^2.

$$u_V = \frac{\rho_L}{G} u_V^* \qquad v_V = \frac{\rho_L}{G} v_V^* \qquad \tau_{ij}^V = \frac{\rho_L D}{\mu_V G} \tau_{ij}^{*L}$$
$$S = \frac{S^*}{D} \qquad R_1 = \frac{R_1^*}{D} \qquad R_2 = \frac{R_2^*}{D}$$

Therefore, Eq. (13) can be written in non-dimensional form as follows:

$$u_L \left(\frac{\partial S}{\partial t} + u_L \frac{\partial S}{\partial z} + v_L \frac{\partial S}{\partial y} \right) - \frac{1}{\mathrm{Re}_L} \left(\tau_{zz}^L \frac{\partial S}{\partial z} + \tau_{yz}^L \frac{\partial S}{\partial y} \right) =$$
$$= \frac{\rho_V}{\rho_L} u_V \left(\frac{\partial S}{\partial t} + u_V \frac{\partial S}{\partial z} + v_V \frac{\partial S}{\partial y} \right) - \frac{1}{\mathrm{Re}_V} \left(\tau_{zz}^V \frac{\partial S}{\partial z} + \tau_{yz}^V \frac{\partial S}{\partial y} \right) - \tag{15}$$
$$- \frac{1}{\mathrm{We}} \left(\frac{1}{R_1} + \frac{1}{R_2} \right) \frac{\partial S}{\partial z}$$

where

$$\mathrm{Re}_L = \frac{GD}{\mu_L} \qquad \mathrm{Re}_V = \frac{GD}{\mu_V} \qquad \mathrm{We} = \frac{G^2 D}{\rho_L \sigma}$$

are the Reynolds numbers for the two phases and the Weber number $\mathrm{We} = \frac{G^2 D}{\rho_L \sigma}$ is the ratio between the kinetic energy and the surface tension. The two-dimensional approximation renders $S = y - \frac{2\delta(z)}{D}$; *ergo* $\frac{\partial S}{\partial z}$ is the rate of change of the annular film thickness δ along the pipe axis, taking into account the heat and mass transfer. The steady-state thickness decreases in the z-direction due to evaporation induced by the wall heat flux.

Given the void fraction, α, in annular flow

$$\alpha = \frac{\pi \left(\frac{D}{2} - \delta \right)^2}{\pi \left(\frac{D}{2} \right)^2} \tag{16}$$

the thickness of the liquid film is expressed as follows:

$$\delta = \frac{D}{2} \left(1 - \sqrt{\alpha} \right) \tag{17}$$

The relationship between quality and void fraction is as follows:

$$\frac{x}{1-x} = \frac{\rho_V}{\rho_L} S_R \frac{\alpha}{1-\alpha} \tag{18}$$

where $S_R = U_V / U_L$. Eq. (18) can be rearranged to determine an explicit function of α

$$\alpha = \frac{x}{\left(1 - \frac{\rho_V}{\rho_L} S_R \right) x + \frac{\rho_V}{\rho_L} S_R} \tag{19}$$

The rate of change of δ along the z-direction is

$$\frac{\mathrm{d}\delta}{\mathrm{d}z} = \frac{\mathrm{d}\delta}{\mathrm{d}\alpha} \frac{\mathrm{d}\alpha}{\mathrm{d}x} \frac{\mathrm{d}x}{\mathrm{d}z} \tag{20}$$

The derivatives are calculated from Eqs. (17), Eq. (19) and Eq. (3), as follows:

$$\frac{\mathrm{d}\delta}{\mathrm{d}\alpha} = -\frac{D}{4\sqrt{\alpha}} \tag{21}$$

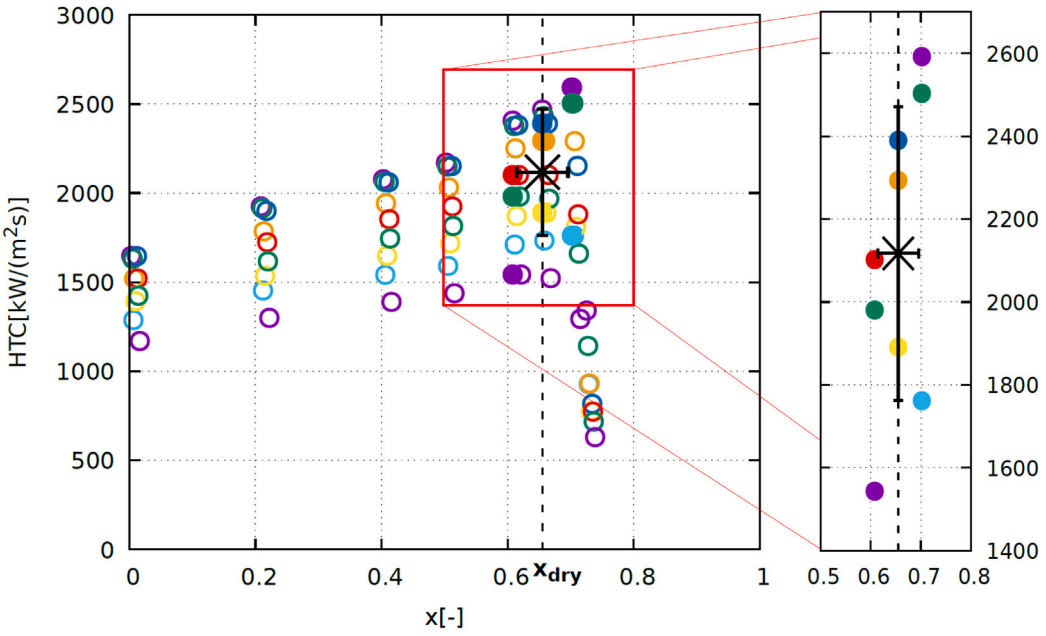

Fig. 11. Determination of dryout vapour quality based on datasets from all installed thermocouples; the open coloured symbols represent different thermocouple locations for an example test case (G = 800 kg/m²s, T_{sat} = −15°C and q = 5 kW/m²), the closed colour symbols identify the determined onset point of dryout for each thermocouple and the dashed line marks the average dryout vapour quality.

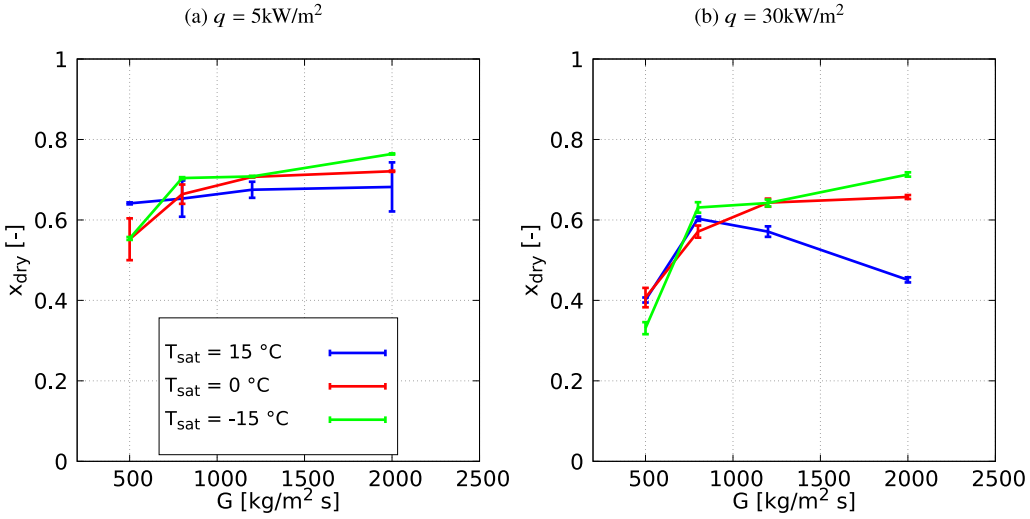

Fig. 12. x_{dry} as a function of G for different q and T_{sat}.

$$\frac{\mathrm{d}\alpha}{\mathrm{d}x} = \frac{\rho_V}{\rho_L} S_R \frac{1}{\left[\left(1-\frac{\rho_V}{\rho_L}S_R\right)x + \frac{\rho_V}{\rho_L}S_R\right]^2} = \frac{\rho_V}{\rho_L} S_R \frac{\alpha^2}{x^2} = \frac{\alpha(1-\alpha)}{x(1-x)} \tag{22}$$

$$\frac{dx}{dz} = \frac{4q}{h_{gl}GD} \tag{23}$$

where $S_R = \frac{x}{1-x}\frac{1-\alpha}{\alpha}\frac{\rho_L}{\rho_V}$ from Eq. (18) and the radius of curvature in the steady flow is

$$R_1 = \frac{D}{2} - \delta = \frac{D}{2}\sqrt{\alpha} \tag{24}$$

Substituting Eqs. (21)–(24) in the last term of Eq. (15), and considering that for the unperturbed interface $R_2 = \infty$, the following expression is obtained:

$$\frac{1}{\mathrm{We}}\left(\frac{1}{R_1}+\frac{1}{R_2}\right)\frac{\partial S}{\partial z} = \frac{2(1-\alpha)}{x(1-x)}\frac{\mathrm{Bo}}{\mathrm{We}} \tag{25}$$

The Boiling number, $\mathrm{Bo} = \frac{q}{h_{gl}G}$ is the ratio between the rate of phase change and the total mass flow rate. As T_{sat} is inversely proportional to h_{gl}, any increase in T_{sat} will correspond to an increase in Bo and consequently a decrease in x_{dry}. The data presented in Fig. 13 showed that the onset of dryout was delayed at decreased saturation temperatures. This effect is attributed to an increase in We. The ratio $\mathrm{Bo/We} = \frac{\rho_L \sigma q}{G^3 h_{gl} D}$ exhibits an inverse proportionality to the mass flux. This mathematical form is consistent with the experimentally-derived δ^+ behaviour, where an inverse proportionality is found between Bo/We and x_{dry}.

The dryout vapour quality x_{dry} is correlated with the right-hand-side of Eq. (25), termed henceforth as the *dryout instability factor* for the δ^+ regime, I_{δ^+}. The dryout instability factor can also be expressed as a function of the slip ratio, $S_R = U_V/U_L$, exploiting Eq. (18):

$$I_{\delta^+} = \frac{2(1-\alpha)}{x(1-x)}\frac{\mathrm{Bo}}{\mathrm{We}} = \frac{2\frac{\rho_V}{\rho_L}S_R}{x^2\left(1-\frac{\rho_V}{\rho_L}S_R\right)+x}\frac{\mathrm{Bo}}{\mathrm{We}} \tag{26}$$

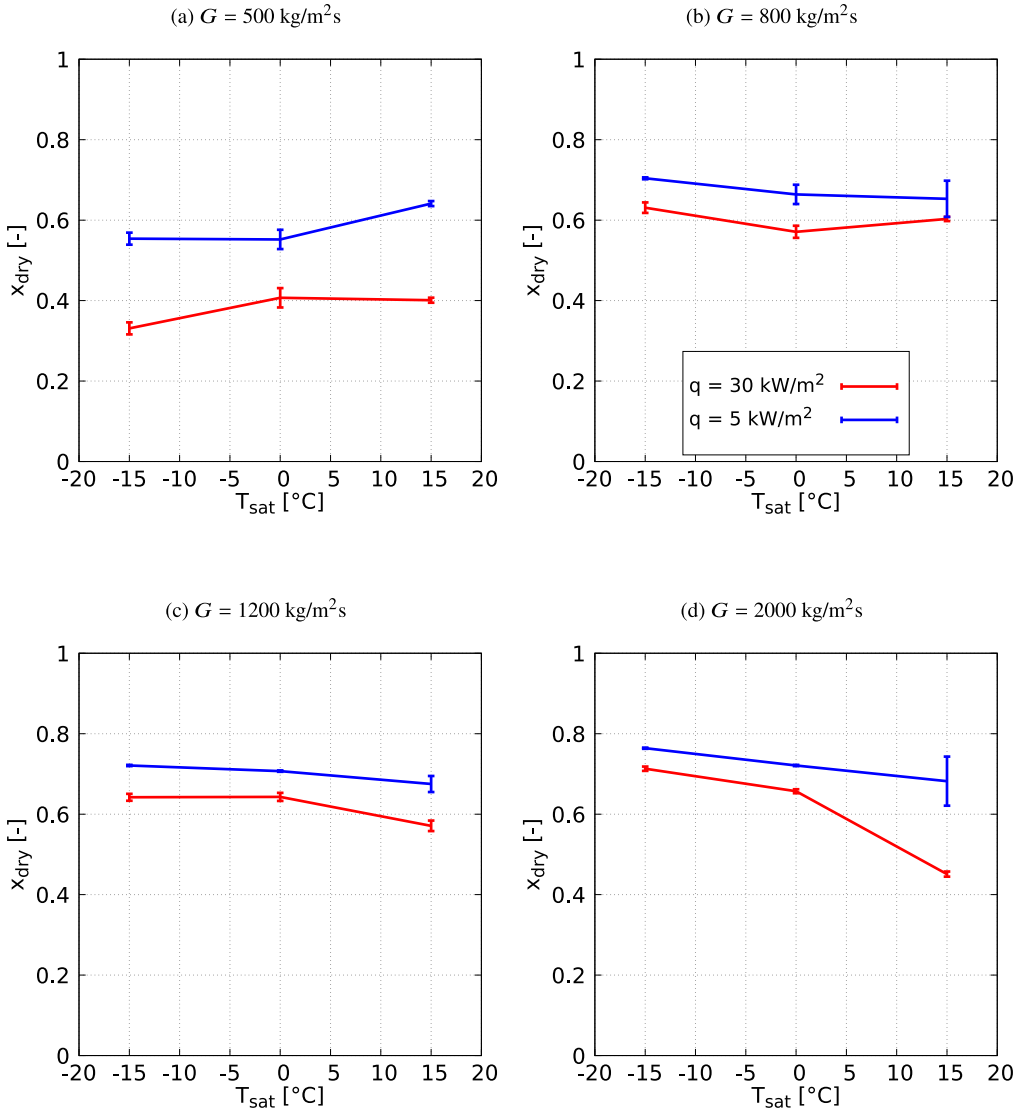

Fig. 13. x_{dry} as function of T_{sat} for different heat flux and G.

Here the slip ratio, S_R, is equal to two, assuming a radially-invariant velocity profile for the vapour core and laminar Couette flow for the liquid film, in accordance with the approach of [28]

Data attributed to the δ^+ regime are reanalysed with respect to the I_{δ^+} parameter and presented as a function of x_{dry} in Fig. 15. I_{δ^+} exhibits a strong dependency on x_{dry} and correlates with an exponential relationship of the form

$$I_{\delta^+} = 10^{-\left(8.96x_{dry}^{3.38}+4.70\right)} \tag{27}$$

where the coefficients were obtained through a least-squares optimisation. Since exponential relationships provide a basis to solve linear problems, the exponential form here supports the authors' hypothesis that dryout is linked to the solution of Eq. (12). Physically, Eq. (26) links the inception of dryout to a threshold over which the forces acting on the liquid-vapour interface (due to the phase change) are strong enough to disrupt the liquid film, which itself is stabilised by the inertia of the flow. The proposed correlation has a coefficient of determination $R^2 = 0.8567$. The coefficient of determination is defined as

$$R^2 = 1 - \frac{\sum_{i=1}^{N}\left(y_i - \hat{y}_i\right)^2}{\sum_{i=1}^{N}\left(y_i - \mu_y\right)^2} \tag{28}$$

where y_i are the collected data, $\hat{y}_i$ are the estimated data and μ_y is the mean of the collected data.

Despite numerous attempts in the literature to develop a *universal* theory for predicting x_{dry}, to the authors' knowledge *all* theories fail to extend their applicability beyond the proposers own datasets. The demonstrated dependency of I_{δ^+} on x_{dry} for the δ^+ regime can be further validated through reproduction of the data from [8]. Fig. 16 shows that the experiments of [8] conform to the new theory.

The coefficients for Ducoulombier's data are different to those in Eq. (27) owing to the 0.5 mm bore pipes used in the experiments; the coefficient of determination for Eq. (29) is $R^2 = 0.77$

$$I_{\delta^+} = 10^{-\left(3.68x_{dry}^{4.70}+4.13\right)} \tag{29}$$

Since the definition of I_{δ^+} contains x_{dry}, an iterative process would be needed to apply Eqs. (27) and (29) for evaporator design purposes. An alternative approach to correlating the data in Fig. 15 employs the Bo/We ratio as the governing parameter, omitting the need for iterative calculation and yielding $R^2 = 0.71$ (see Fig. 17):

$$\frac{\mathrm{Bo}}{\mathrm{We}} = 10^{-\left(7.25x_{dry}^{3.25}+4.94\right)} \tag{30}$$

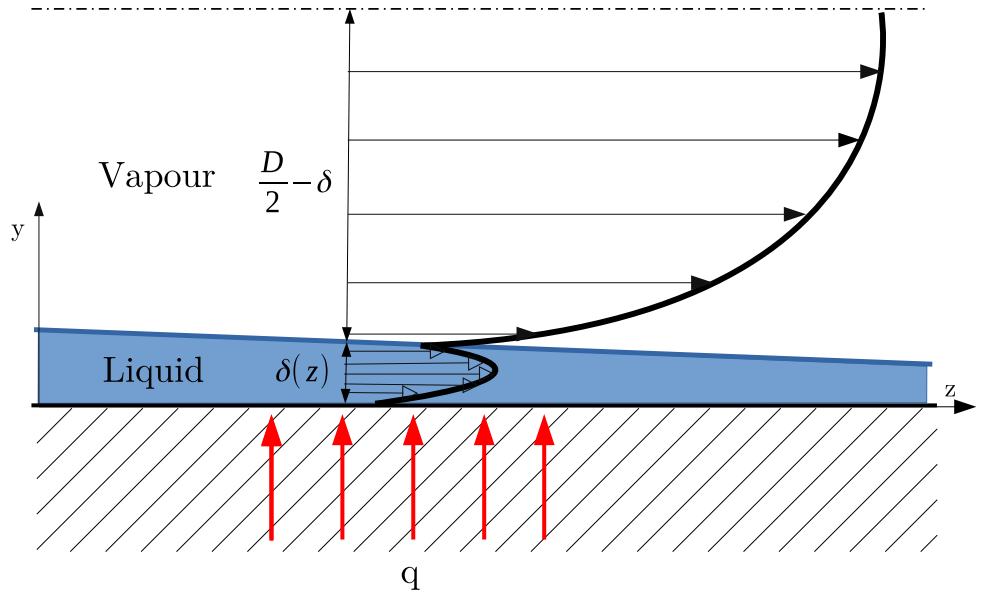

Fig. 14. Schematic of two-dimensional annular flow for a pipe with internal diameter D under a heat flux q. δ is the thickness of the liquid film as a function of the axial coordinate z.

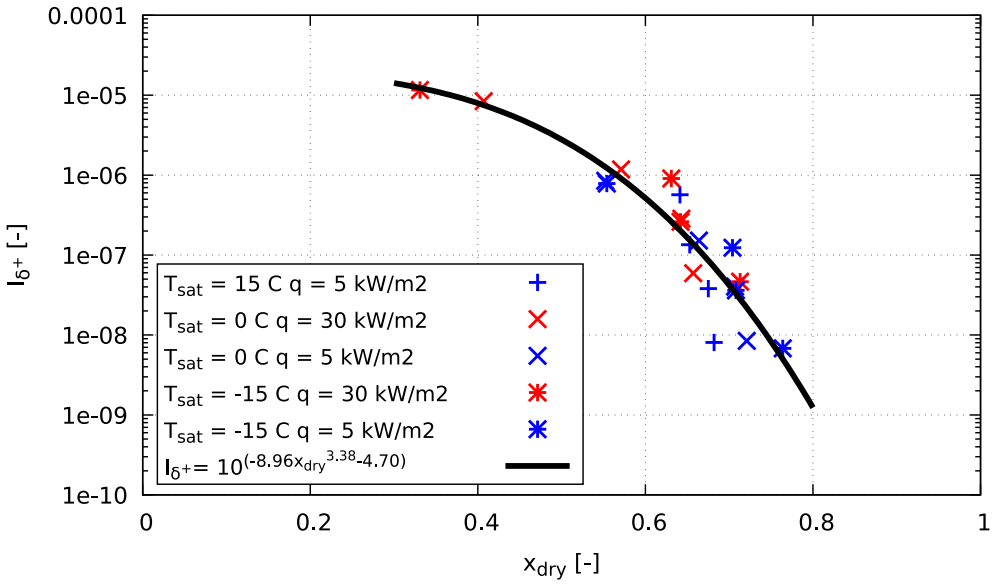

Fig. 15. I_{δ^+} as a function of x_{dry}; all data are for a 1 mm pipe bore, $S_R = 2$.

A Bo/We correlation is also proposed for the experiments of [8] (see Fig. 18)

$$\frac{\text{Bo}}{\text{We}} = 10^{-(3.22x_{dry}^{5.2}+4.13)} \tag{31}$$

with $R^2 = 0.69$.

The results generated in this study can be exploited to produce flow pattern maps for two-phase CO_2. Flow pattern maps are typically used to identify the physical state of the flow at a specific condition, from which appropriate correlations can predict associated pressure drops and heat transfer rates. The most widely recognised flow pattern map for CO2 was produced by [12], whom assembled flow regimes for fixed diameter pipes at constant saturation temperature and heat flux. Considering D = 1 mm, T_{sat} = −15° C and q = 5 kW/m^2, the flow pattern map proposed by [12] is shown in Fig. 19(a). The red line marks the inception of dryout; the green points are the dryout vapour qualities determined in this study. The flow map proposed by Cheng fails to predict the dryout behaviour when the δ^+ regime dominates. A modified flow pattern map is presented as Fig. 19(b) utilising the Bo/We correlation proposed in this paper. Herein lies the significance of such a correlation, where the independence from T_{sat} and q enables the experimenter to conduct investigations at a single value of the aforementioned quantities, while permitting extrapolation of the trends to a general parameter set.

4. Conclusions

This study presents a new method for predicting the inception of dryout in milliscale pipe flows through evaluating the Heat Transfer Coefficient (HTC) in boiling CO_2 flow at saturated conditions. The investigation is based on an extensive experimental campaign at CERN, underpinned by a new approach to modelling the dryout vapour quality. The principal conclusions from this study are as follows:

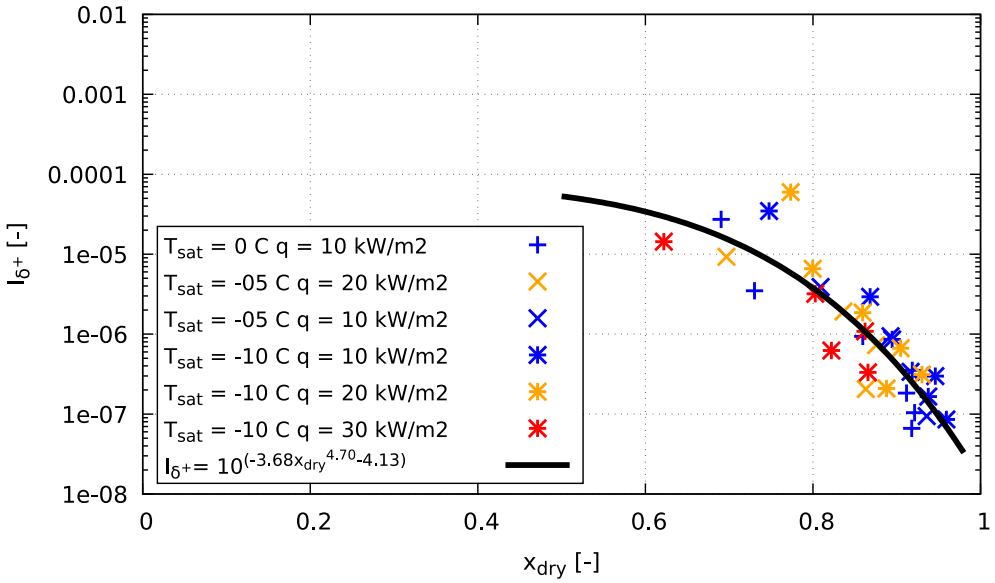

Fig. 16. Reproduction of the data from [8], converted to I_{δ^+} as a function of x_{dry}; all data are for a 0.5 mm pipe bore, $S_R = 2$.

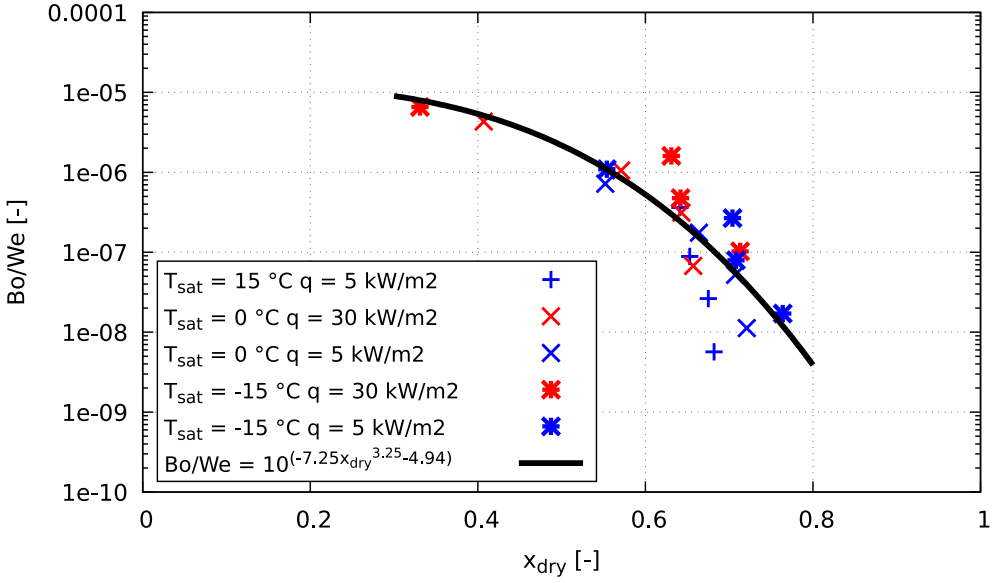

Fig. 17. Bo/We as a function of x_{dry}; all data are for a 1 mm pipe bore.

Analysis of the heat transfer coefficient:

- *Influence of mass flux, G*: At the fully saturated liquid condition, the level of HTC is independent of mass flux. This behaviour is attributed to nucleate boiling occurring in low vapour quality flow regimes. The independence of HTC with mass flux seen for the saturated liquid condition, is equally observed as conditions approach the onset of dryout — exclusively for cases at *elevated* saturation temperatures. At negative values of T_{sat}, no independence with mass flux is observed beyond the saturated liquid condition.
- *Influence of heat flux, q*: As the experiments are carried out at saturated conditions, the temperature of the fluid is constant and equal to the saturation temperature, *i.e.* it is not affected by the level of heat flux. *Ergo* the experiments exhibit proportionality between HTC and q.
- *Influence of saturation temperature, T_{sat}*: For conditions at high vapour quality, the level of HTC increases due to convective evaporation. This effect is magnified at lower T_{sat}, where HTC exhibits a strong positive correlation with dryout vapour quality, prior to the onset of dryout; for low T_{sat} the correspondingly lower vapour density results in a higher flow velocity enhancing the local convective heat transfer. Lowering the saturation temperature shifts the dominant behaviour from nucleate boiling to convective boiling.

Inception of dryout:

- *Influence of heat flux, q*: For all cases, earlier inception of dryout exists for the higher heat flux condition.
- *Influence of saturation temperature T_{sat}*: For the lowest mass flux, the dryout vapour quality broadly increases with T_{sat} for all tested heat fluxes. For higher mass fluxes the trend progressively reverses. At the lowest mass flux condition a lower saturation temperature results in earlier onset of dryout.

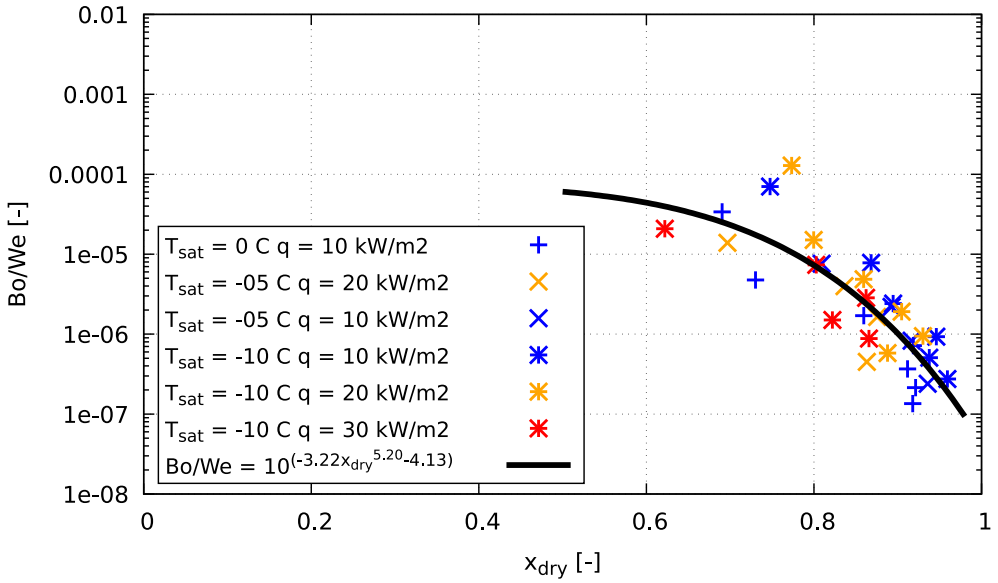

Fig. 18. Reproduction of the data from [8], converted to Bo/We as a function of x_{dry}; all data are for a 0.5 mm pipe bore.

(a) Map of Cheng et al. (2008) (b) New map with Bo/We correlation

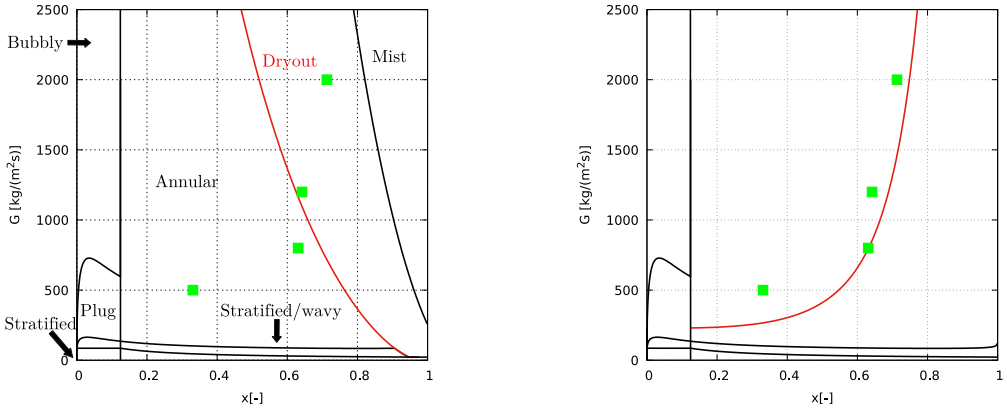

Fig. 19. Flow pattern maps for internal D = 1 mm, $T_{sat} = -15°$ C and $q = 30$ kW/m^2.

Stability analysis for the δ^+ regime:

- Stability analysis at the liquid-vapour interface is employed successfully to predict the dryout vapour quality based on the dryout instability factor in the δ^+ regime, I_{δ^+}. An exponential correlation is used to predict I_{δ^+} as a function of dryout vapour quality, with the coefficients dependent only on pipe diameter.
- An alternative approach to correlating the data employs the Bo/We ratio as the governing parameter, omitting the need for iterative calculation of dryout vapour quality.
- The proposed correlation is independent from T_{sat} and q, enabling the experimenter to conduct investigations at a single value of the aforementioned quantities, while permitting extrapolation of the trends to a general parameter set.

The strong dependence of x_{dry} on I_{δ^+} identifies the stability of the liquid-vapour interface as the principal governing variable for the dryout phenomenon in the δ^+ regime. This study provides theory to interpret the δ^+ regime for dryout, validated with specifically-acquired data and the wider literature. The proposed correlation, based on a physically-informed parameter form the theoretical model, is independent from the saturation temperature and heat flux, enabling robust design of carbon-dioxide evaporator architectures from data acquired at a single value of the aforementioned quantities. The versatility of this new framework is unique.

CRediT authorship contribution statement

Giulio Cantini: Writing – review & editing, Writing – original draft, Methodology, Investigation, Formal analysis, Data curation, Conceptualization. **Desiree Hellenschmidt:** Writing – review & editing, Supervision, Methodology, Data curation. **Camila Pedano:** Writing – review & editing, Supervision, Investigation, Data curation. **Paolo Petagna:** Writing – review & editing, Writing – original draft, Supervision, Methodology, Data curation. **Carl Sangan:** Writing – review & editing, Writing – original draft, Resources, Methodology. **Mauro Carnevale:** Writing – review & editing, Writing – original draft, Validation, Methodology, Funding acquisition, Conceptualization.

Declaration of competing interest

The authors declare that they have no known competing financial interests or personal relationships that could have appeared to influence the work reported in this paper.

Acknowledgment

We thank the international research grant (Grant number IES\R1\221141) of the Royal Society and Andrew Langley for his technical assistance.

Data availability

Data will be made available on request.

References

[1] P. Gullo, K. Tsamos, A. Hafner, Y. Ge, S. Tassou, State-of-the-art technologies for transcritical R744 refrigeration systems–a theoretical assessment of energy advantages for European food retail industry, Energy Procedia 123 (2017) 46–53.

[2] D. Kotliński, The CMS pixel detector, Nucl. Instruments Methods Phys. Res. Sect. A: Accel. Spectrometers, Detect. Assoc. Equip. 465 (1) (2001) 46–50, http://dx.doi.org/10.1016/S0168-9002(01)00345-X, SPD2000 URL https://www.sciencedirect.com/science/article/pii/S016890020100345X.

[3] V. Vrba, The ATLAS pixel detector, Nucl. Instruments Methods Phys. Res. Sect. A: Accel. Spectrometers, Detect. Assoc. Equip. 465 (1) (2001) 27–33, http://dx.doi.org/10.1016/S0168-9002(01)00342-4, SPD2000 URL https://www.sciencedirect.com/science/article/pii/S0168900201003424.

[4] P. Tropea, J. Daguin, P. Petagna, H. Postema, B. Verlaat, L. Zwalinski, CO2 evaporative cooling: The future for tracking detector thermal management, Nucl. Instruments Methods Phys. Res. Sect. A: Accel. Spectrometers, Detect. Assoc. Equip. 824 (2016) 473–475, http://dx.doi.org/10.1016/j.nima.2015.08.052, Frontier Detectors for Frontier Physics: Proceedings of the 13th Pisa Meeting on Advanced Detectors URL https://www.sciencedirect.com/science/article/pii/S0168900215010165.

[5] S. Ghiaasiaan, Two-Phase Flow, Boiling, and Condensation: In Conventional and Miniature Systems, second ed., Cambridge University Press, 2007.

[6] G. Hewitt, Annular Two-Phase Flow, Elsevier, 2013.

[7] S.-M. Kim, I. Mudawar, Universal approach to predicting saturated flow boiling heat transfer in mini/micro-channels – Part I. Dryout incipience quality, Int. J. Heat Mass Transfer 64 (2013) 1226–1238, http://dx.doi.org/10.1016/j.ijheatmasstransfer.2013.04.016, URL https://www.sciencedirect.com/science/article/pii/S0017931013003219.

[8] M. Ducoulombier, S. Colasson, J. Bonjour, P. Haberschill, Carbon dioxide flow boiling in a single microchannel–Part II: Heat transfer, Exp. Therm. Fluid Sci. 35 (4) (2011) 597–611.

[9] R. Revellin, P. Haberschill, J. Bonjour, J. Thome, Conditions of liquid film dryout during saturated flow boiling in microchannels, Chem. Eng. Sci. 63 (24) (2008) 5795–5801.

[10] R. Yun, Y. Kim, Critical quality prediction for saturated flow boiling of CO2 in horizontal small diameter tubes, Int. J. Heat Mass Transfer 46 (14) (2003) 2527–2535, http://dx.doi.org/10.1016/S0017-9310(03)00036-X, URL https://www.sciencedirect.com/science/article/pii/S001793100300036X.

[11] L. Wojtan, T. Ursenbacher, J. Thome, Investigation of flow boiling in horizontal tubes: Part I—A new diabatic two-phase flow pattern map, Int. J. Heat Mass Transfer 48 (14) (2005) 2955–2969, http://dx.doi.org/10.1016/j.ijheatmasstransfer.2004.12.012, URL https://www.sciencedirect.com/science/article/pii/S0017931005000268.

[12] L. Cheng, G. Ribatski, J. Moreno Quibén, J. Thome, New prediction methods for CO2 evaporation inside tubes: Part I – A two-phase flow pattern map and a flow pattern based phenomenological model for two-phase flow frictional pressure drops, Int. J. Heat Mass Transfer 51 (1) (2008) 111–124, http://dx.doi.org/10.1016/j.ijheatmasstransfer.2007.04.002, URL https://www.sciencedirect.com/science/article/pii/S0017931007002839.

[13] Y. Qiu, D. Garg, L. Zhou, C. Kharangate, S.-M. Kim, I. Mudawar, An artificial neural network model to predict mini/micro-channels saturated flow boiling heat transfer coefficient based on universal consolidated data, Int. J. Heat Mass Transfer 149 (2020) 119211.

[14] D. Hellenschmidt, P. Petagna, Effects of saturation temperature on the boiling properties of carbon dioxide in small diameter pipes at low vapour quality: Heat transfer coefficient, Int. J. Heat Mass Transfer 172 (2021) 121094.

[15] R.W. Morse, J. Chan, E.T. Hurlburt, J.-M. Le Corre, A. Berson, G.F. Nellis, K.M. Dressler, A new paradigm for the role of disturbance waves on film dryout and wall heat transfer in annular two-phase flow, Int. J. Heat Mass Transfer 219 (2024) 124812, http://dx.doi.org/10.1016/j.ijheatmasstransfer.2023.124812, URL https://www.sciencedirect.com/science/article/pii/S0017931023009572.

[16] D. Hellenschmidt, P. Petagna, Effects of saturation temperature on the boiling properties of carbon dioxide in small diameter pipes at low vapour quality: Pressure drop, Int. J. Heat Mass Transfer 163 (2020) 120209.

[17] D. Hellenschmidt, Experimental Studies on Small Diameter Carbon Dioxide Evaporators for Optimal Silicon Pixel Detector Cooling (Ph.D. thesis), Bonn U., 2020.

[18] B. Verlaat, Controlling a 2-phase CO2 loop using a 2-phase accumulator, in: International Conference of Refrigeration, Citeseer, 2007.

[19] B. Verlaat, L. Zwalinski, R. Dumps, M. Ostrega, P. Petagna, T. Szwarc, TRACI, a multipurpose CO2 cooling system for R&D, in: 10th IIR Gustav Lorentzen Conference on Natural Refrigerants, 2012.

[20] H. Coleman, W. Steele, Experimentation, validation, and uncertainty analysis for engineers, John Wiley & Sons, 2018.

[21] H.-K. Oh, H.-G. Ku, G.-S. Roh, C.-H. Son, S.-J. Park, Flow boiling heat transfer characteristics of carbon dioxide in a horizontal tube, Appl. Therm. Eng. 28 (8–9) (2008) 1022–1030.

[22] C. Ong, J. Thome, Macro-to-microchannel transition in two-phase flow: Part 1 – Two-phase flow patterns and film thickness measurements, Exp. Therm. Fluid Sci. 35 (1) (2011) 37–47, http://dx.doi.org/10.1016/j.expthermflusci.2010.08.004, URL https://www.sciencedirect.com/science/article/pii/S0894177710001500.

[23] R. Morse, T. Moreira, J. Chan, K. Dressler, G. Ribatski, E. Hurlburt, L. McCarroll, G. Nellis, A. Berson, Critical heat flux and the dryout of liquid film in vertical two-phase annular flow, Int. J. Heat Mass Transfer 177 (2021) 121487, http://dx.doi.org/10.1016/j.ijheatmasstransfer.2021.121487, URL https://www.sciencedirect.com/science/article/pii/S0017931021005901.

[24] P. Drazin, W. Reid, Hydrodynamic stability, Cambridge University Press, 2004.

[25] K. Adham-Khodaparast, M. Kawaji, B. Antar, The Rayleigh–Taylor and Kelvin–Helmholtz stability of a viscous liquid–vapor interface with heat and mass transfer, Phys. Fluids 7 (2) (1995) 359–364.

[26] T. Funada, D. Joseph, Viscous potential flow analysis of Kelvin–Helmholtz instability in a channel, J. Fluid Mech. 445 (2001) 263–283, http://dx.doi.org/10.1017/S0022112001005572.

[27] R.E. Kelly, The stability of an unsteady Kelvin—Helmholtz flow, J. Fluid Mech. 22 (3) (1965) 547–560, http://dx.doi.org/10.1017/S0022112065000964.

[28] R. Miesen, G. Beijnon, P. Duijvestijn, R. Oliemans, T. Verheggen, Interfacial waves in core-annular flow, J. Fluid Mech. 238 (1992) 97–117, http://dx.doi.org/10.1017/S0022112092001654.

[29] L. Preziosi, K. Chen, D. Joseph, Lubricated pipelining: stability of core-annular flow, J. Fluid Mech. 201 (1989) 323–356, http://dx.doi.org/10.1017/S0022112089000960.

[30] H. Schlichting, J. Kestin, Boundary Layer Theory, vol. 121, Springer, 1961.

[31] A. Davey, P.G. Drazin, The stability of Poiseuille flow in a pipe, J. Fluid Mech. 36 (2) (1969) 209–218, http://dx.doi.org/10.1017/S0022112069001613.

[32] S. Orszag, Accurate solution of the Orr–Sommerfeld stability equation, J. Fluid Mech. 50 (4) (1971) 689–703, http://dx.doi.org/10.1017/S0022112071002842.